PHYSICAL REVIEW B VOLUME 56, NUMBER 6 1 AUGUST 1997-II

Optical studies of Cr^{3+} in $KMgF_3$: Time-resolved site-selective spectroscopy and experimental evidence of spin-orbit coupling

M. Mortier,* Q. Wang, J. Y. Buzaré, and M. Rousseau
Laboratoire de Physique de l'Etat Condensé, CNRS URA 807, Université du Maine, Avenue O. Messiaen, 72017 Le Mans Cedex, France

B. Piriou
Laboratoire PCM, CNRS URA 1907, Ecole Centrale des Arts et Manufactures, Grande Voie des Vignes,
92295 Châtenay-Malabry Cedex, France

(Received 27 January 1997; revised manuscript received 3 April 1997)

Three different sites of the Cr^{3+} ions in the fluoride perovskite $KMgF_3$ have been identified by absorption, selective optical excitation, and time-resolved emission spectroscopy of the $^4T_2 \leftrightarrow {}^4A_2$ transition. High-pressure measurements showing the crossover from low-crystal field to high-crystal field, allows us to situate the Dq/B values of the different chromium sites clearly below 2.3. The different spin-orbit components associated with the zero-phonon lines of the $^4T_2 \leftrightarrow {}^4A_2$ transition of each type of site are clearly shown on the optical spectra and identified by group-theory analysis. The decay profiles of the $^4T_2$ level are exponential and the lifetimes at 15 K are 903, 919, and 473 μs for the cubic, quadratic, and trigonal sites, respectively. The trigonal center which presents the lowest energy levels was peculiarly studied. Emission and excitation spectra are compared; their evolution versus temperature is followed and explained by the thermal population of the different spin-orbit sublevels. The phonon sideband of the trigonal site is compared with our previous lattice dynamic studies of the pure compound. The different peaks of the emission broadband are described in terms of phonons of the matrix and normal modes of the $[CrF_6]^{3-}$ complex. [S0163-1829(97)03430-9]

I. INTRODUCTION

In the $3d$ transition-metal ions, most of the visible and near-infrared electronic transitions are strongly coupled with phonons. Then, the emission and excitation associated spectra present vibronically broadened bands. This coupling is of a great practical interest for the manufacture of tunable solid-state lasers operating at room temperature. However, the extent of the phonon spectrum of a material is also a strong promoter of nonradiative transitions which are strongly negative for laser efficiency. In such a case, it is advisable to choose compounds with a low cutoff frequency of phonons with regard to the energy gap between the electronic levels of the active ion. In this framework, the fluoride compounds, which present a cutoff frequency of phonons lower than $600\ \mathrm{cm}^{-1}$, are good candidates.

Since the work of Brauch and Durr,[1] in 1984, which has shown laser operation in $KZnF_3$:Cr^{3+}, many spectroscopic studies have been done on the fluoride perovskites. In particular, the cubic and stable perovskites $KMgF_3$ and $KZnF_3$ have been well investigated by electron paramagnetic resonance (EPR) for Cr^{3+}.[2–7] The different studies have concluded the existence of four unequivalent sites for trivalent chromium impurities.

$KMgF_3$ has the standard perovskite structure belonging to the $(O_h^1 - Pm3m)$ space group with $a = 3.973$ Å. Its structure is scheduled stable by many criterions[8,9] and in fact no phase transition has been observed in this compound. The Mg^{2+} ion has a ionic radius of 0.86 Å and is replaced substitutionally by the Cr^{3+} ion ($r = 0.76$ Å) in a $(1b)$ octahedral site. Because of the charge difference between the Mg^{2+} ion and Cr^{3+} ion, several charge compensation mechanisms required for electrical neutrality lead to different crystal-field sites for the substituted Cr^{3+} ions. The first and most probable case is a nondistorted site, the charge compensation being farther in the crystal. The second most probable case is an axially distorted site along a [111] axis due to a K^+ vacancy in $(1a)$ of the same cell, resulting in a C_{3v} symmetry site. The least probable site is distorted along the [100] axis due to a Mg^{2+} vacancy in the neighboring cell (C_{4v} symmetry).[1,2] Another quadratic site is cited but not clearly interpreted and never optically observed in $KZnF_3$ crystals.[3]

With excitation and high-pressure emission measurements at RT, we show that the chromium ions in $KMgF_3$ present a low-crystal-field behavior, clearly below the $^4T_2$-^2E level crossing situated at $Dq/B = 2.3$, even for distorted sites. After, the usual spectroscopic parameters of the chromium ions will be deduced.

Up to now, many optical studies have been devoted to Cr^{3+}-doped $KMgF_3$ (Ref. 10) and $KZnF_3$.[1,3,11–13] To our knowledge, there is no unambiguous identification of the three different Cr^{3+} crystal-field sites in $KMgF_3$ through their emission and excitation spectra. To clarify this situation, we present a site-selective experiment which allows us to separate the response of the three different Cr^{3+} sites. Furthermore, the corresponding spin-orbit components of the three sites are very well observed on emission and excitation spectra and identified through a group-theory study. Previously, they had been wrongly attributed to R lines by Lee, Han, and Henderson.[10]

Then, we propose an opposite point of view to the interpretations of Lee, Han, and Henderson about the optical properties of Ni^{2+} and Cr^{3+} codoped $KMgF_3$ crystal. Indeed,

0163-1829/97/56(6)/3022(10)/$10.00

in their paper, they assume that the Cr^{3+} ions substituting without local charge compensation on the octahedral Mg^{2+} site give rise, at 300 K, to a broadband $^4T_2 \rightarrow {}^4A_2$ emission, which results from the thermal occupancy of an excited $^4T_2$ state just above the ^2E level which, at lower temperature, gives rise to emission in R line. We show that these observed sharp lines are in fact due to spin-orbit splitting of the axially perturbed $^4T_2$ level. They assume that both octahedral and trigonal centers occupy crystal-field sites near degeneracy of the ^2E-$^4T_2$ levels and that the tetragonal site lies in low crystal field. Their misinterpretations were probably due to crystal codoping and the resulting band overlap between Ni^{2+} and Cr^{3+} ions. In contrast, during our present and previous works,[14] we have studied crystals doped either with Ni^{2+} or Cr^{3+}. We can then assume the absence of any ambiguity in our attributions.

We particularly study the trigonally distorted site because its levels are lying clearly below the levels of the other sites. Then, we can be sure to obtain its own emission. We follow the evolution of the emission spectrum with temperature. After time-resolved site-selective spectroscopy, we measure the fluorescence lifetime of each site. Finally, the low-temperature emission spectrum is interpreted in terms of phonons of the pure compound and normal modes of the octahedral entity $[CrF_6]^{3-}$.

II. EXPERIMENTAL

$KMgF_3$ being a congruent melting compound, the raw material before doping has been synthesized by the Bridgman-Stockbarger method from a stoichiometric melt $KF+MgF_2$ in a cylindrical graphite crucible of 30 mm diameter. This first crystallization was done to obtain a higher purity sample using segregation mechanism. The starting materials used were KF Merck ($>99\%$) and MgF_2 Merck Patinal powder. The crucible includes a 4 mm diameter tip in order to select a spontaneous seed. The crucible was placed in a thermal gradient with the tip in the low-temperature range. The crystal was grown with a temperature rate of 3 °C/h from 1120 °C (50 °C higher than the fusion temperature) down to the end of the growth. A pure single crystal of good optical quality was obtained. The sample had easy cleavage planes along {100}.

The crystal growth of the Cr^{3+}-doped $KMgF_3$ has also been made using the Bridgman Stockbarger method in a sealed platinum crucible. The starting material was the pure $KMgF_3$ previously crystallized and reduced in small crystallites. The melt was doped with 1% molar (CrF_3+KF) mixture. After classical growth, the resulting crystal was clear and of green homogeneous color. A sample of high optical and crystalline quality was cut from this block and Laüe oriented ($2\times2\times4$ mm).

Excitation spectrum at room temperature was obtained by exciting the samples with light from a 150 W Xe lamp passed through a 0.22 m monochromator. A R928 Hamamatsu photomultiplier, placed at the exit slit of 0.34 m monochromator, was used to measure the luminescence which was analyzed at 753.2 nm. The mean resolution of the excitation spectrum was 5 nm.

For the high-pressure emission measurements, the pressure was generated with an anvil cell whose inox gasket had been pretended before being drilled. The cylindrical chamber is 100 μm high and has a 100 μm diameter. The sample was immersed with a ruby in an hydrostatic pressure medium consisting of a 4:1 methanol-ethanol solution. Pressure calibration was carried out through the pressure shift of the R lines of ruby. The fluorescence was analyzed with a Dilor-Z24 triple-monochromator Raman microspectrometer after excitation at 514.5 nm. The mean resolution was 5 cm^{-1}.

The high-resolution emission measurements were done, after excitation by the 457.9 nm line of a 80 mW CW argon laser used in the light regulation mode, with a Dilor Z24 triple monochromator equipped with a R928 Hamamatsu cooled photomultiplier and a photon counting chain. A He close-cycle Leybold cryogenerator was used to obtain temperatures between 300 and 10 K. The mean resolution width was about 1.5 cm^{-1}. The absorption spectrum was recorded at 8.5 K with an average resolution of 0.1 nm on a Cary 5E from Varian.

The high-resolution excitation spectra were recorded at 8.5 K using a dye laser (Blue Nile) excited by 8 ns pulses of a frequency doubled Nd:YAG laser. The detector was an Hamamatsu R929S photomultiplier placed at the exit slit of a Coderg double monochromator spectrometer. The mean resolution was 4 cm^{-1}.

III. RESULTS AND DISCUSSION

A. Optical excitation at room temperature

At RT, the excitation, or absorption, spectrum exhibits three main bands corresponding to the spin-allowed electronic transitions from the $^4A_2$ to the $^4T_2$, $^4T_1(^4F)$ and $^4T_1(^4P)$ levels. The absorption or excitation spectra appear as broadbands which reflect electronic transitions accompanied by the simultaneous creation or annihilation of one or several phonons. Table I summarizes the data and selection rules concerning the purely electronic transitions in a perfect octahedral site. We indicate the electronic configuration of the different levels involved in the transitions and the position of the associated broadband maxima. The axial distortions and lattice vibrations can then be considered as perturbations.

In spite of the dipole magnetic (DM) forbidden character of their zero-phonon line (ZPL), the $^4A_2 \rightarrow {}^4T_1(^4F)$ and $^4A_2 \rightarrow {}^4T_1(^4P)$ absorption bands are easily observed because many Cr^{3+} ions occupy some sites of lowest symmetry, either from a static point of view or from a dynamic one, due to lattice vibrations. The $^4A_2 \rightarrow {}^4T_2(^4F)$ band exhibits singularities (dips) due to Fano antiresonances[15] with the $^2E(^2G)$ and $^2T_1(^2G)$ levels.

B. Emission spectrum at room temperature under hydrostatic pressure

In order to verify the exact position of the ^2E level with respect to the $^4T_2$ level and then the crystal-field situation, we recorded RT emission spectrum of $KMgF_3$:Cr^{3+} versus hydrostatic pressure (Fig. 1). We can easily observe that a sharp line appears around 15 100 cm^{-1} at a pressure higher than 6 GPa. When increasing the pressure from 8 up to 16 GPa, the intensity of the emission broadband decreases and the intensity of the sharp line increases. This sharp line, due

TABLE I. Data and selection rules concerning the purely electronic transitions in perfect octahedral site with position of the absorption band's maxima.

	Absorption				
Transition	$^4A_{2g}\rightarrow{}^4T_{2g}$	$^4A_{2g}\rightarrow{}^4T_{1g}$	$^4A_{2g}\rightarrow{}^4T_{1g}$	$^4A_{2g}\rightarrow{}^2E_g$	$^4A_{2g}\rightarrow{}^2T_{1g}$
Ground level	$^4A_{2g}(^4F)$ $L=3,\ S=3/2$ t_{2g}^3				
Excited level	$^4T_{2g}(^4F)$	$^4T_{1g}(^4F)$	$^4T_{1g}(^4P)$	$^2E_g(^2G)$	$^2T_{1g}(^2G)$
	$L=3,\ S=3/2$	$L=3,\ S=3/2$	$L=1,\ S=3/2$	$L=4,\ S=1/2$	$L=4,\ S=1/2$
Configuration	$t_{2g}^2e_g^1$	$t_{2g}^2e_g^1$	$t_{2g}^1e_g^2$	t_{2g}^3	t_{2g}^3
ΔS	0	0	0	1	1
$DM+DE$	Allowed	Forbidden	Forbidden	Forbidden	Forbidden
Position (nm)	660	458	297		

to the ^2E level, is accompanied with strong Stokes and anti-Stokes phonon replicas noted S and AS, respectively. At RT, the width of the R line is greater than the gap between the R_1-R_2 spin-orbit components of the ^2E electronic level with the result that R lines are not separated. These observations are typical of a crossover from low-field to high-field behavior due to a progressive enhancement of the crystal-field strength with increasing pressure. In low-crystal-field, Cr^{3+} ions exhibit a broadband ($^4T_2\rightarrow{}^4A_2$) fluorescence instead of a narrow band ($^2E\rightarrow{}^4A_2$) emission of high crystal-field sites, such as ruby. The broadband emission persists up to higher pressures with diminishing intensity, as a consequence of thermal population of the $^4T_2$ state from the ^2E state. A mixing between the wave functions of these two states can be also considered.[16] So, opposite to Lee,[10] we can conclude that $Dq/B<2$ for the Cr^{3+} ions in $KMgF_3$.

From the position of the absorption bands and of the ^2E and $^2T_1$ levels, we can evaluate the usual spectroscopic parameters: the Dq crystal-field parameter and the covalency quenched free-ion Racah parameters B and C. In fact, despite common use, it is not correct to take the maximum of the absorption bands to determine the crystal-field situation in Tanabe-Sugano diagrams,[17] because they relate only to pure electronic transitions.[18,19] As a result, a large error is made on the position of vibronically coupled levels, due to Stokes shift (more than $1000\ \mathrm{cm}^{-1}$), the error being negligible with ^2E level. But, in order to give comparable data with others works, we still use the maxima and in a second time we will estimate the error so produced. From the expression of the energy levels given by Lever[20] in the case of octahedral sites, we obtain the values of the different absorptions:

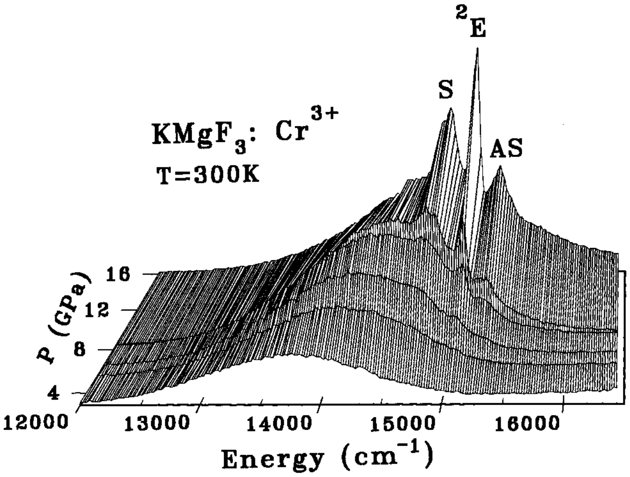

FIG. 1. $^4T_2$ emission broadband and ^2E sharp line in the emission spectrum of $KMgF_3$ versus hydrostatic pressure at 300 K. The anti-Stokes and Stokes phonon replicas are noted AS and S.

$$E_1[^4A_2\rightarrow{}^4T_2(^4F)]=10Dq, \tag{1}$$

$$E_2[^4A_2\rightarrow{}^4T_1(^4F)]=7.5B+15Dq-0.5(225B^2+100Dq^2-180DqB)^{1/2}, \tag{2}$$

$$E_3[^4A_2\rightarrow{}^4T_1(^4P)]=7.5B+15Dq+0.5(225B^2+100Dq^2-180DqB)^{1/2}. \tag{3}$$

With the overestimated data ($E_1=15\,150$, $E_2=21\,930$, and $E_3=33\,650\ \mathrm{cm}^{-1}$), there is no unique solution for the three relationships (1), (2) and (3). Nevertheless, by using the graphical method,[7,14] the best fit values are $Dq=1450\ \mathrm{cm}^{-1}$, $B=760\ \mathrm{cm}^{-1}$, and $Dq/B=1.9$. Then, the C parameter value can be evaluated using the expression of the ^2E level emission:

$$E(^2E\rightarrow{}^4A_2)=9B+3C-\frac{50B^2}{10Dq}=15\,100\ \ \mathrm{cm}^{-1} \quad \text{(high-pressure value)}. \tag{4}$$

We can also use the expression of the $^2T_1$ level, because this level has been observed at $16\,188\ \mathrm{cm}^{-1}$ as the Fano antiresonance in low-temperature excitation spectrum:

$$E(^4A_2\rightarrow{}^2T_1)=9B+3C-\frac{24B^2}{10Dq}. \tag{5}$$

We obtain a mean value of $C=3426\ \mathrm{cm}^{-1}$. Finally, $B=760\ \mathrm{cm}^{-1}$ and $C=3426\ \mathrm{cm}^{-1}$ are the free-ion values[17] ($B=918\ \mathrm{cm}^{-1}$, $C=4133\ \mathrm{cm}^{-1}$) reduced by a factor of 0.83 reflecting covalency effect in this compound. These values seem to be consistent because the C/B ratio of the free ion is kept in the crystal. In $KZnF_3{:}Cr^{3+}$, the covalency correction factor was 0.79.[11]

From the maximum of the absorption band of the $^4T_2$ level and the position of the barycenter of its ZPL (Sec. III D), we can evaluate the Stokes shift to about $1200\ \mathrm{cm}^{-1}$. Using this value and the maximum of the absorption bands, we can then estimate the position of the other

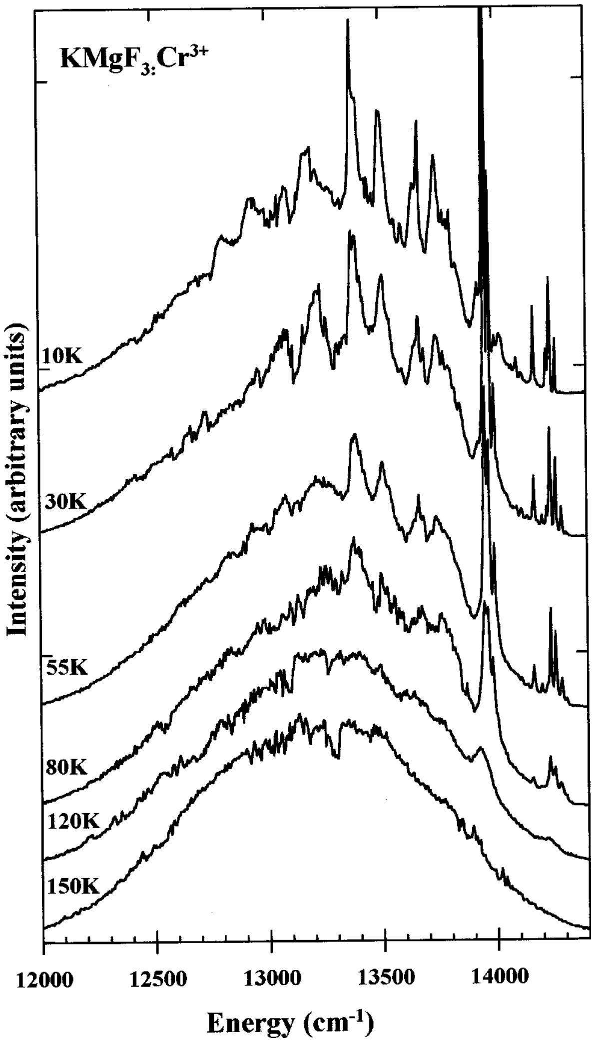

FIG. 2. High-resolution emission spectrum versus temperature recorded after excitation at 457.9 nm (21 839 cm^{-1}) in the ${}^4T_1({}^4F)$ band. Slit width 1.5 cm^{-1}.

phonon coupled electronic levels: ${}^4T_1({}^4F)$: 20 630 cm^{-1} and ${}^4T_1({}^4P)$: 32 470 cm^{-1}. Then, with the same calculation method,[7,14] we obtain $Dq = 1410\ cm^{-1}$, $B = 718\ cm^{-1}$, and finally $Dq/B = 2$ giving an error of 5%. The relative error is larger for low crystal-field compounds such Ni^{2+}-doped compounds[18] for which Dq/B is smaller than 1.

C. High-resolution emission spectrum versus temperature

We report the ${}^4T_2 \rightarrow {}^4A_2$ emission spectrum recorded from 150 to 10 K (Fig. 2). The spectra between 300 and 150 K do not show any noticeable variation in shape or intensity. When decreasing the temperature, sharp lines appear. Under 80 K, very strong and sharp lines, probably purely electronic lines, appear. At 10 K, the intensity of the ZPL at around 13 950 cm^{-1} become very high. This line is truncated on the figure. Many other sharp lines exist on this spectrum, even though only one ZPL is expected for each site of the chromium ion. In $KZnF_3$:Cr^{3+}, many studies had presented only one ZPL for each site on the emission spectra.[1,3] These spectra will be discussed in the next section.

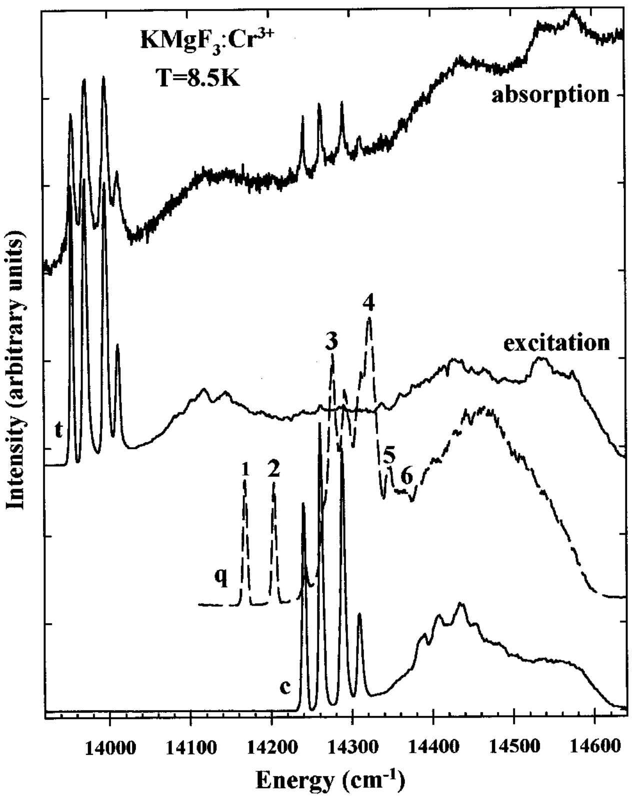

FIG. 3. Absorption spectrum recorded at 8.5 K with a resolution of 0.1 nm. Time-resolved excitation spectra of the trigonal (t), quadratic (q), and cubic (c) sites of Cr^{3+} at 8.5 K observed at 13 954, 14 168, and 14 240 cm^{-1}, respectively. Slit width 4 cm^{-1}.

In this case, the ${}^2E$ level lies just above the ${}^4T_1$ level and is drained by nonradiative transitions toward the lower level ${}^4T_1$. In order to verify this assertion, we have carried out low-temperature absorption and excitation measurements.

D. Low-temperature absorption and excitation spectra of the ${}^4T_2$ level

Now, we try to interpret the structure of the levels descended from ${}^4A_2$ and ${}^4T_2$ by analyzing the low-temperature emission and excitation spectra. We just report the absorption spectrum, between 13 900 and 14 600 cm^{-1}, corresponding to the purely electronic lines range. In the spectrum of Fig. 3, we can see two groups of four sharp lines around 14 000 and 14 300 cm^{-1}. The attribution of the groups of lines to the different sites is proposed in accordance with previous work in similar families of crystals[1,3,21] even if some of them have not evidenced spin-orbit coupling. These groups can be attributed to the most probable sites, i.e., trigonal and cubic sites, respectively. Indeed, according to the stabilization energies of transition-metal ions in distorted sites, the energy levels of the axially distorted sites are lower than those of the cubic site.[22] So, the lowest levels are attributed to the trigonal site.

We can observe that the integrated intensity below the four sharp lines of these two sites is greater for the trigonal one. In fact, the integrated intensity results of the product of the number of ions by the cross section is related to the selection rules. For the cubic sites, the electric dipole transition is forbidden by the Laporte rule when it is allowed for the axially distorted sites. Knowing that electric dipole (ED) transitions are of very high intensity in comparison with the

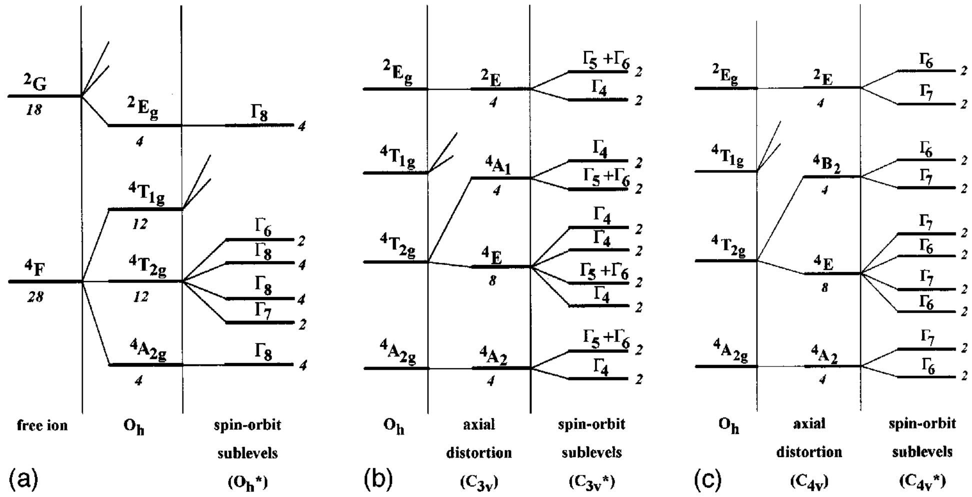

FIG. 4. (a) Crystal-field and spin-orbit splitting of the useful electronic levels in undistorted octahedral site. (b) and (c) crystal-field and spin-orbit splitting in axially distorted sites: trigonal and quadratic.

magnetic dipole (MD) transition, it is obvious that the cubic sites (MD) are probably more numerous than the trigonal ones. The absence of line ascribed to quadratic sites (ED allowed) indicates their low content in the crystal. Nevertheless, other weak sharp lines were revealed on emission spectra at low temperature. These new lines and the previous ones were used to separate the proper response of each site by excitation spectroscopy. These spectra are also reported on the same figure. The quadratic site is now observed but, only three of the four sites observed by EPR are evidenced. The emission was fixed at the position of the lowest zero-phonon line of each site. Using time-resolved spectroscopy, we were able to record the emission spectrum even on the excitation line without any perturbation.

The existence of many lines in each group associated with one Cr^{3+} site could be due to the existence of spin-orbit coupling on the $^4T_2$ level. But, in no case can these lines be associated with $^2E \rightarrow {}^4A_2$ emission expected at $15\,100\ \mathrm{cm}^{-1}$ after high-pressure experiments. Indeed, the energy difference between the ^2E and $^4T_2$ levels (ZPL around $14\,000\ \mathrm{cm}^{-1}$ in Fig. 1) is about $1100\ \mathrm{cm}^{-1}$. This difference between the two electronic levels confirms that $Dq/B<2$ unlike the conclusion of Lee.[10] We can affirm that all the Cr^{3+} sites are low-crystal field. Moreover, the EPR studies[2] have not shown such strong intensity of the axial distortion.

In the case of the $3d^N$ ions, the crystal-field term in the Hamiltonian is much greater than the spin-orbit coupling term. Nevertheless, this latter interaction can be observed as a splitting of ZPL at low temperatures. The effective spin-orbit Hamiltonian is $H_{\mathrm{so}}=\lambda \mathbf{L}\cdot\mathbf{S}+\mu(\mathbf{L}\cdot\mathbf{S})^2$ where L is the effective angular momentum ($L=1$) for a T_2 state and S is the total spin.

For the free ion, the representation of the generic state ^{2S+1}L, $(2S+1)(2L+1)$ degenerated, is given by $D_L \otimes D_S$. Placed in the crystal, the representations of the ion are reduced in terms of irreducible representations of the symmetry group of the site (G_c): $D_L=\Sigma_i c_i \Gamma_i$ (only D_L is reduced) giving the states: $\Gamma_i \otimes D_S \Leftrightarrow {}^{2S+1}\Gamma_i$, e.g., ^4F state in the O_h group: $D_3 \otimes D_{3/2} \rightarrow (A_2+T_2+T_1)\otimes D_{3/2} \rightarrow {}^4A_2+{}^4T_2+{}^4T_1$. Obviously, the spin multiplicity in each component is kept. These states are of even parity because the $3d$ electrons have an orbital quantum number equal to 2. So, we would better write $^4A_{2g}+{}^4T_{2g}+{}^4T_{1g}$.

Then the spin-orbit interaction results in the generic representations $\Gamma_i \otimes D_S$ becoming reduced in terms of irreducible representations of the symmetry group (G_c):$\Gamma_i \otimes D_S = \Sigma_k \Gamma_k$. Moreover, the spin being half-integer, we must use the double group $(G_c)^*$ associated with the group (G_c); e.g., the representation of the spin D_S in the double group (O_h^*) is then Γ_6 for $D_{1/2}$ and Γ_8 for $D_{3/2}$. The five electronic levels corresponding to the A_1, A_2, T_1, T_2, E symmetries ($\Gamma_1, \Gamma_2, \Gamma_3, \Gamma_4, \Gamma_5$), respectively, become coupled spin-orbit levels described by the Γ_6, Γ_7, and Γ_8 symmetries.

The successive splittings of the five orbital electronic levels corresponding to the A_1, A_2, E, T_1, T_2 symmetries are presented in Fig. 4(a) for the O_h group (cubic site). Figure 4 summarizes the group-theory analysis for the electronic levels useful for our interpretations and the lines are only guides for the eyes. The peaks of the excitation spectrum are labeled according to the O_h double-group irreducible representations (Table II).

In the case of distorted sites, it is convenient to correlate the symmetry distortions to the O_h symmetry group. In $(C_{4v})^*$, the double point group associated with C_{4v}, the $D_{3/2}$ representation is reduced as follows:[23] $D_{3/2}=D_{1/2}(\Gamma_6)$

TABLE II. Assignment of the observed spin-orbit ZPL of the cubic site with their positions.

	Cubic site (O_h):$^4T_2$			
$L \cdot S$ sublevels	Γ_7	Γ_8	Γ_8'	Γ_6
ω (cm^{-1})	14 240	14 261	14 288.5	14 309.5

TABLE III. Assignment of the observed spin-orbit ZPL of the trigonal site with their positions.

	Trigonal site (C_{3v}):^4E			
$L \cdot S$ sublevels	Γ_4	$\Gamma_5+\Gamma_6$	Γ_4'	Γ_4''
ω (cm^{-1})	13 954	13 971	13 996	14 011.5

TABLE IV. Assignment of the observed spin-orbit ZPL of the quadratic site with their positions.

	Quadratic site (C_{4v}):$^4B_2$,^4E					
	$^4B_2$		^4E			
$L\cdot S$ sublevels	Γ_7	Γ_6	Γ_7	Γ''_7	Γ'_6	Γ''_6
label on Fig. 3	1	2	3	4	5	6
ω (cm^{-1})	14 168	14 204	14 277	14 322.5	14 346.5	14 380

$\oplus\Gamma_7$. Similarly, in the C^*_{4v} point group: $D_{3/2}=D_{1/2}(\Gamma_4)\oplus\Gamma_5\oplus\Gamma_6$ in which Γ_5 and Γ_6 are Kramers conjugate states. The representations of the O_h group are reduced in terms of representations of the C_{3v} or C_{4v} group before taking into account spin-orbit splitting. The splittings corresponding to the trigonal and quadratic sites are presented in Figs. 4(b) and 4(c).

We have used some numeric calculations of the spin-orbit levels of the octahedral Cr^{3+} ion versus the intensity of axial distortions presented by De Viry,[21] in order to obtain a correct attribution of each $L\cdot S$ component. In the cubic sites (without any distortion), we can observe four lines when only three are expected with first-order spin-orbit coupling. Consequently, the Γ_8 and Γ_6 $L\cdot S$ components are separated, which proves a second-order spin-orbit interaction. In accordance with De Viry calculations, we propose the attribution of the different lines of the excitation spectra given in Tables II, III, and IV. For the quadratic site, the different lines are labeled from 1 to 6 in Fig. 3, as in Table IV, in order to make the interpretation easier. The splittings between the lines are consistent with the previous results concerning the cubic site in $KZnF_3$:Cr^{3+},[11,12] and the order of magnitude of splittings in $Na_3Li_3In_2F_{12}$:Cr^{3+}.[21]

With trigonal or quadratic distortions, the $^4A_2$ ground level is split into two components but we do not observe any additional splitting of the sharp lines. In fact, some studies[11,24] have shown that the spin-orbit splitting of the ground level is less than 0.5 cm^{-1} for d^3 ions in octahedral trigonally distorted symmetry and is consequently not resolved within our experimental configuration.

All the spin-orbit sublevels have been observed through their emission or excitation lines. For the trigonal site, we can remark that the barycenter of the four spin-orbit sublevels associated with the ^4E level (lowest component of the trigonally split $^4T_2$ level) lies 300 cm^{-1} below the cubic one. In such a case, the two spin-orbit sublevels of the $^4A_1$ trigonal one (other component of the $^4T_2$ level) are predicted to be 500 cm^{-1} higher than the cubic levels. They have not been observed. For the tetragonal site, the six $L\cdot S$ sublevels of $^4B_2$ and ^4E (from $^4T_2$) have the same barycenter as the cubic components but with an additional splitting. The position of the ZPL of $^4T_2$ level lies clearly below the ^2E level (15 100 cm^{-1}) even for the most distorted site.

E. Temperature dependence of emission and excitation spectra of the $^4T_2$ level

We now compare detailed emission and excitation spectra of a selected site (Fig. 5) in order to verify the exact nature of the lines. The trigonal site was chosen since it is easy to

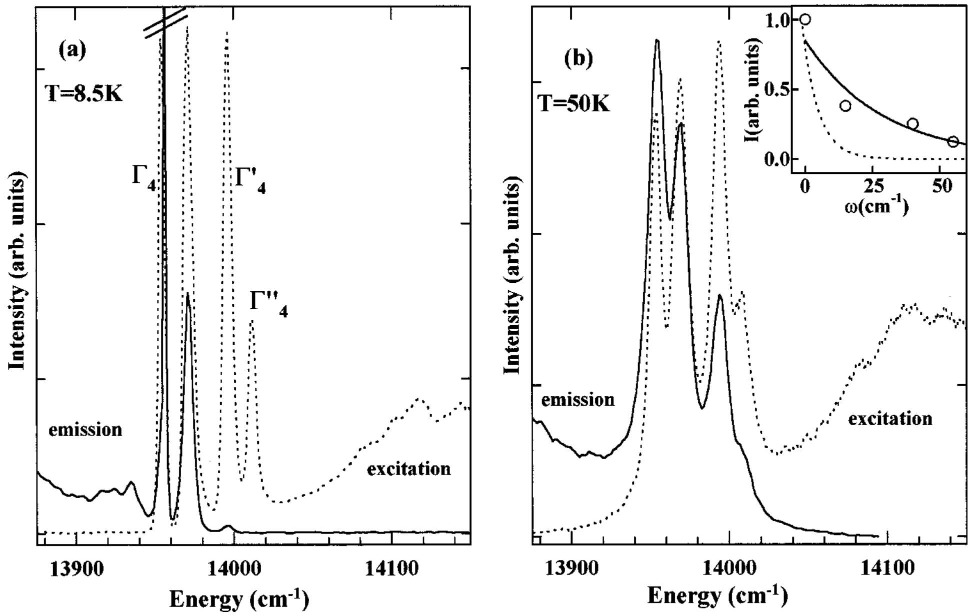

FIG. 5. (a) Emission spectrum of the trigonal site at 8.5 K after 13 954 cm^{-1} excitation with a resolution of 4 cm^{-1}. The dotted line indicates the excitation spectrum of the trigonal site at 8.5 K with emission fixed at 13 955 cm^{-1}. (b) Same spectra recorded at 50 K but with a resolution of 6 cm^{-1} for the emission spectrum. Inset: integrated intensity of the spin-orbit lines reported versus their relative position to the lowest one Γ_4: $\Delta\omega_i=\omega(\Gamma_i)-\omega(\Gamma_4)$. The continuous line corresponds to the law at 41.5 K described in the text, the dotted line is the law at 8.5 K.

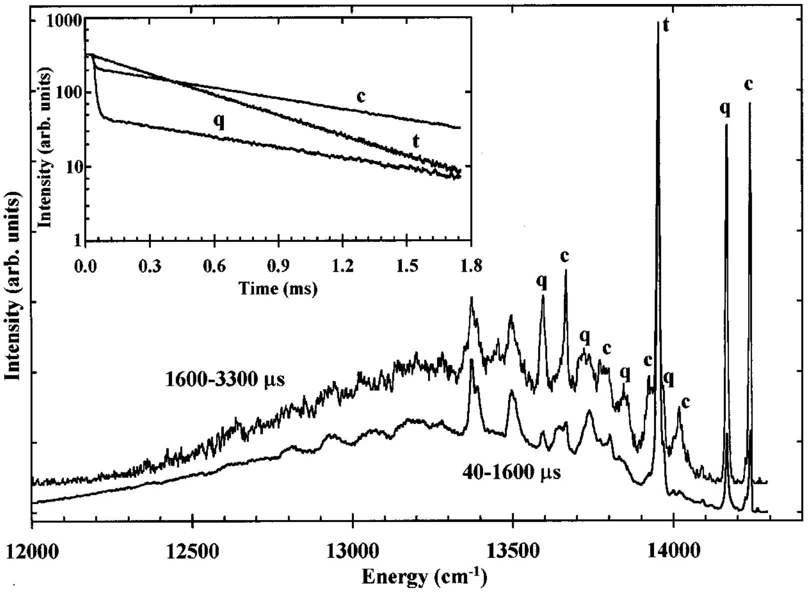

FIG. 6. Time-resolved spectrum recorded at 8.5 K after excitation at 14 322 cm^{-1} with a resolution of 6 cm^{-1}. The bold solid line indicates the first time window corresponding to the intensity integrated between 40 and 1600 μs after the excitation pulse. The thin line is the second window (1600–3300 μs). The c, q, and t labels correspond to cubic, quadratic, and trigonal contributions. Inset: luminescence decay profiles of the three sites after selective excitation recorded at 8.5 K. Their lifetimes are $\tau_t = 473\,\mu$s, $\tau_c = 903\,\mu$s, and $\tau_q = 919\,\mu$s.

discriminate because its spin-orbit levels are the lowest in energy of the three sites. The excitation spectrum in Fig. 5(a) is part of the spectrum on Fig. 3. The emission spectrum has been achieved after selective excitation in the Γ_4 line (13 954 cm^{-1}) at 8.5 K. The mean resolution was 4 cm^{-1}. The same lines appear on the excitation and emission spectra, so they are ZPL. But the only clearly observed lines in emission at 8.5 K are those of lowest energy. Even when trying to obtain emission from the highest levels after resonant excitation of each one, we never get any emission arising from the Γ_4'' sublevel. Emission spectrum is independent of the excited component. It presents a very small intensity from the Γ_4', a noticeable intensity from the Kramers doublet $(\Gamma_5+\Gamma_6)$ and, of course, a very strong intensity of the Γ_4 (lowest) sublevel.

In order to verify the idea of thermal populating of the different sublevels, we present in Fig. 5(b), the same emission and excitation spectra recorded at 50 K. This time, we can observe the four lines on the emission spectrum. On the contrary, when observed by excitation, the relative intensities of the four lines are constant with temperature and only an homogenous broadening of the lines is observed when the temperature increases. The simulation of the experimental emission spectrum with Gaussian shapes allows us to calculate the integrated intensities of these lines. They are reported versus their relative position to the lowest $L\cdot S$ level Γ_4: $\Delta\omega_i = \omega(\Gamma_i) - \omega(\Gamma_4)$ [inset in Fig. 5(b)]. We can compare the measured values to a thermal populating law of the sublevels corrected by the oscillator strength f_{Γ_i} as follows:

$$I(\Delta\omega_i) = \frac{f_{\Gamma_i} g_i e^{-\hbar\Delta\omega_i/kT}}{\sum_{i=1}^{4} g_i e^{-\hbar\Delta\omega_i/kT}} \tag{6}$$

with g_i the degeneracy of the state Γ_i ($g_i = 2$ for the considered sublevels). The oscillator strengths are measured on the excitation spectrum and normalized on Γ_4. In fact, for commodity reasons, the measured integrated intensities are reported divided by the oscillator strength and then the continuous line corresponds to $I(\Delta\omega_i)/f_{\Gamma_i}$. The measured values are in fine agreement with the model [inset in Fig. 5(b)] but indicates a real temperature of 41.5 K instead of the 50 K given by the thermal regulator.

For 8.5 K, we have not measured the integrated intensity, the ZPL being of very high intensity and probably truncated during experiment. We can just evaluate $I(\Gamma_5+\Gamma_6)/I(\Gamma_4) \approx 10\%$, Γ_4' nearly equal to zero but observed and Γ_4'' not observed. In the meantime, the order of magnitude is correct, compared with the thermal populating law [curve in the dotted line in the inset of Fig. 5(b)].

We can then conclude that the observed spectra result of the emission from the ${}^4T_2$ level split by axial distortion (${}^4E$ and ${}^4A_1$) and spin-orbit interaction with a thermal equilibrium between the different sublevels: Γ_4, $(\Gamma_5+\Gamma_6)$, Γ_4' and Γ_4''. This equilibrium is confirmed by the lifetimes as seen in the next section.

F. Low-temperature time-resolved emission from ${}^4T_2$

In Fig. 6, we present the time-resolved emission spectrum from ${}^4T_2$ recorded at 8.5 K after excitation at 14 322 cm^{-1}, just in the ${}^4A_2 \rightarrow {}^4E(\Gamma_7'')$ transition of the tetragonal site. This selective excitation enhances its emission but the majority of cubic and trigonal sites still remain excited. Delay and time gates (see the caption) have been chosen in order to separate the sites of different lifetimes. Thus, the curve in the bold solid line represents the emission of the trigonal site of the short lifetime essentially and the other one those of the quadratic and cubic sites of the long lifetime. In fact, the lifetime of the quadratic and cubic sites are so close that, despite many attempts, we have never succeeded in the separation of their two spectra by time-resolved spectroscopy. This seems to be associated with the magnitude of the distortions. The trigonal site corresponds to a K^+ vacancy in the same cell. The $L\cdot S$ sublevels are 300 cm^{-1} below those of the cubic site. Using numerical calculations,[21] we could evaluate an intensity of distortion of about 600 cm^{-1}. The quadratic distortion is smaller because the Mg^{2+} vacancy is in the neighboring cell when it is in the same cell for the trigonal case. The associated spin-orbit sublevels are near those of the cubic site. We could thus evaluate the intensity[21] of the quadratic distortion to about 100 cm^{-1}. The selection rules are then probably more affected by the trigonal distortion resulting in a lifetime quite different from those of the two other sites.

In Fig. 6, we have attributed several replica of the second curve to the cubic (c) or quadratic (q) sites using their energy difference compared to the ZPL of each site. This was done with respect to the energy differences measured on the trigonal site spectrum.

G. Low-temperature luminescence decays

In the inset of Fig. 6, we have plotted the decay profiles of the three sites after selective excitation. The decay of the trigonal site has been recorded on a vibronic replica (13 381 cm^{-1}) after ${}^4E(\Gamma_4)$ excitation at 13 954 cm^{-1}. It appears purely exponential, with no sign of transfer, giving a lifetime of 473 μs. The very high intensity of the Γ_4 ZPL of the trigonal site and its relatively short lifetime agree with an allowed electric dipole transition due to strongly distorted site.

The decays of the cubic (c) and quadratic (q) sites are quite similar, i.e., 903 and 919 μs, respectively, after their selective excitation. The profiles of decay are perturbed by the exciting line for the short times (<0.1 ms) because they are obtained with resonant excitation. The decays have been also measured on the different spin-orbit lines of each site. No difference of lifetime between the $L \cdot S$ sublevels of a given site has been observed, which confirms the thermal equilibrium previously demonstrated.

For higher temperatures, it is not possible to separate the different sites and only a mean value has been measured. At 77 K, the lifetime of the emission broadband was of 475 and 370 μs at 300 K; this decrease being due to the thermal enhancement of nonradiative processes. The different luminescence lifetimes are relatively long for a ${}^4T_2$ level, but previously observed in different fluoride crystals.[6,11,21] Indeed, we must consider the effects of electron-lattice interaction and spin-orbit coupling of the doublet and quartet states.[25] They introduce an electronic wave-function mixing of the ${}^4T_2$ state with the ${}^2E$ long-lived state. Moreover, the phonon cutoff frequency of the fluoride compounds being lower than that of the oxide ones, the probability of nonradiative transitions is weaker in fluorides. So, a long decay of the ${}^4T_2$ level in $KMgF_3$ is not surprising.

H. Vibronic emission of the trigonal center

After the study of the localized electronic levels of the Cr^{3+} impurities, it is advisable to take into account the dynamical properties of the matrix. We have peculiarly studied the emission of the trigonal site because its electronic levels lie clearly below the other ones. After excitation in the Γ_4 ZPL, the spectrum was recorded at 8.5 K. The emission (Fig. 7) is mainly due to the phonon replica of the lowest energy spin-orbit line Γ_4, the only level which is thermally populated, of the ${}^4E({}^4T_2)$ level (Fig. 4). This spectrum results from both vibronic couplings with the phonons of the matrix and with the normal modes of the $[CrF_6]^{3-}$ complex.

Many works take into account only the modes whose wave vector is equal to zero, i.e., the modes situated at the center of the first Brillouin zone. But, such considerations lead to a discontinuous optical spectrum with a discrete distribution of replicas. It is easy to see that the vibronically broadened transitions are continuous, at least with an intermediate or strong electron-phonon coupling. The problem of the energy-momentum conservation rule is easily resolved by the defect itself. Indeed, due to the presence of a defect, the translation symmetry is lost and the whole Brillouin zone is folded at the Γ point. Consequently, all the vibration modes of the matrix can interact with the defect.[14]

TABLE V. Assignment of the peaks of the trigonal site vibronic emission band, with their energies and frequencies.

Peak	Energy (cm^{-1})	Frequency (cm^{-1})	Assignment	Reference
1	13 996		Γ_4' ZPL	This work
2	13 971		$(\Gamma_5+\Gamma_6)$ ZPL	This work
3	13 954	0	Γ_4 ZPL	This work
4	13 829	125	$R_{25}-M_3$ flat branch	32
5	13 804	150	$M_2'-R_{15}-M_5'$ flat branches	32
6	13 788	166	TO_1 LR mode	33
7	13 759	195	LO_1 IR mode	33
8	13 741	213	$t_{2u}[CrF_6]^{3-}$	3, 34
9	13 654	300	TO_2 IR mode	33
10	13 644	310	$t_{1u}[CrF_6]^{3-}$	3, 34
11	13 589	365	LO_2 IR mode	33
12	13 497	457	$e_g[CrF_6]^{3-}$ and TO_3 IR mode	3, 33, 34
13	13 392	562	$a_{1g}[CrF_6]^{3-}$	3, 34
14	13 372	582	$t_{1u}[CrF_6]^{3-}$	3, 34

Moreover, when the electronic states of an impurity in a crystal are coupled to the vibrations of the lattice, this coupling is commonly represented as arising from a cluster of ions next to the impurity.[26,27] Then, the Cr^{3+} ion and its surrounding octahedron may be considered as a molecular complex. This effect is more efficient for the chromium ion than other $3d$ ions, like Ni^{2+}, because of its stronger covalency.[7,14] The normal modes of the $[CrF_6]^{3-}$ complex come from the reducible representation: $\Gamma_{vib}=a_{1g}+e_g+t_{2g}+2t_{1u}+t_{2u}(O_h)$. Moreover, these modes can be decomposed by the symmetry lowering of the octahedra due to the charge compensations caused by the substitution of Mg^{2+} by Cr^{3+} ions. So, we can interpret the emission spectrum in terms of phonons of the pure compound and normal modes of the octahedral entity $[CrF_6]^{3-}$.

In Table V, we propose an attribution of the 14 peaks labeled in Fig. 7. The first three are the three spin-orbit sublevels observed at low temperature; they are purely electronic lines. The first phonon replicas (4 and 5), lying at low frequency, i.e., up to about 160 cm^{-1} of the Γ_4 line, are due to flat branches of the phonon-dispersion curves of $KMgF_3$.[28] They correspond to the $R_{25}-M_3$, $R_{15}-M_5'$ and $R_{15}-M_2'$ branches giving sharp peaks in the phonon density of states. The peaks labeled 6, 7, 9, and 11 correspond to the frequency of infrared modes of the $KMgF_3$ matrix.[29] They also give sharp peaks in the density of states. The peaks labeled 8, 10, 12, 13, and 14 may be attributed to $[CrF_6]^{3-}$ normal modes. Their frequencies belong to the classical values generally found for such complexes[3,30] in different crys-

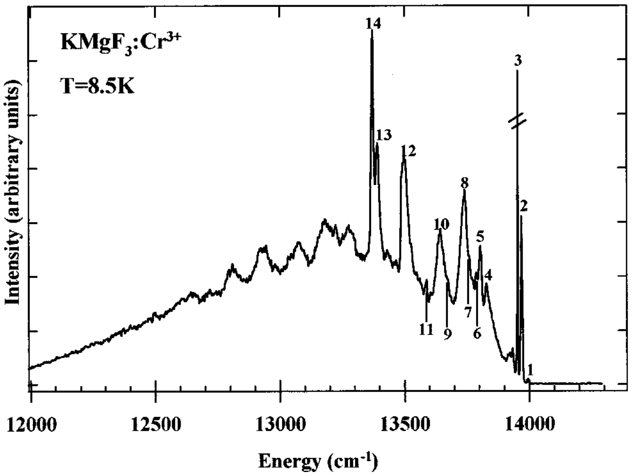

FIG. 7. Emission spectrum of the selected trigonal site at 8.5 K after excitation in the Γ_4 ZPL (labeled 3) with a resolution of 4 cm^{-1} (line 3 is truncated). The assignment of the labeled peaks is in Table V.

tals. The dips between the different peaks correspond to dips in the phonon density of states. Especially, the dips between the 8th and 9th peaks and just before the 11th peak correspond, respectively, to a hole and a pseudogap in the density of states.

The t_{2u} and e_g modes of $[\mathrm{CrF}_6]^{3-}$, respectively, situated at 213 and 457 cm^{-1} are resonant modes,[31] because their frequencies lie in the middle of the optic band of KMgF$_3$. The t_{1u} mode situated at 310 cm^{-1}, lies clearly in the vicinity of the pseudogap, between TO$_2$ and LO$_2$ modes, in the phonon density of states. It is consequently a gap mode.[31] The a_{1g} and t_{1u} modes at 562 and 582 cm^{-1} are true localized modes because their frequencies are higher than the frequency cutoff, corresponding to the LO$_3$ mode at 551 cm^{-1}.[28] The frequency of a gap mode does not belong to the frequencies of the normal modes of the crystal, but lies below the cutoff frequency of the crystal. Therefore, the gap mode is less well localized than the high-frequency local mode. We can observe that the two localized modes give very sharp and strong replicas (13, 14), when the resonant or gap mode gives rise to broader replicas.

Beyond 600 cm^{-1} below the Γ_4 ZPL, i.e., the 14th peak, the replicas are due to the combination of several phonons. The attribution is then more difficult and may be questionable.

In our assignment of the different lines in the emission spectrum, we have neglected the effect of the trigonal distortion on the normal modes of the $[\mathrm{CrF}_6]^{3-}$ complex. In fact, the t_{2g} irreducible representation of the O_h group is reduced in a_1+e, irreducible representations of the C_{3v} group, in the same way $t_{1u}=a_2+e$ and $t_{2u}=a_1+e$.

IV. CONCLUSION

After description of the crystal growth, we have briefly recalled the structure and doping condition of the perovskite KMgF$_3$. With excitation measurements and emission spectrum under high pressure, we have estimated the usual spectroscopic parameters of the chromium ions in the compound. A crossover from low crystal field to high crystal field has been obtained with high-pressure measurements. The low-crystal-field situation is now clearly established for the Cr^{3+} with $Dq/B=1.9$ (<2.3), resulting in the $^4T_2 \rightarrow ^4A_2$ emission, opposite to the results of Lee, Han, and Henderson.[10] The crystal-field parameter is $Dq=1450\ \mathrm{cm}^{-1}$ and the Racah parameter $B=760\ \mathrm{cm}^{-1}$. The C parameter has been evaluated to 3426 cm^{-1}. These values are the free-ion parameters covalency quenched with a reducing factor of 0.83. Using the position of the maximum of the absorption bands instead of ZPL introduces an error of 5% on the exact value of Dq/B.

With low-temperature spectra, we present the evolution of the vibronically broadened $^4T_2 \rightarrow ^4A_2$ transition. The absorption spectrum at low temperature shows clearly the trigonal and cubic sites. We have observed, by excitation, the spectra of three sites and clearly evidenced a spin-orbit coupling through the splittings of the purely electronic transitions. An assignment of the different $L \cdot S$ lines has been done from a group-theory analysis. We have compared the excitation and emission spectra in order to evidence the ZPL. We have shown the evolution of the emission spectrum with temperature results of a thermal equilibrium between the different $L \cdot S$ sublevels.

We have measured the fluorescence lifetime of each site: 473 μs for the trigonal site, 903 and 919 μs for the cubic and quadratic sites. The strong difference of lifetime and energy position of the electronic levels of the trigonal site indicates a strong axial distortion.

Finally, the low-temperature emission spectrum has been interpreted in terms of phonons of the pure compound. The positions of the replicas of the ZPL were compared with the peaks of the density of states associated with the flat branches of the phonon-dispersion curves measured at 300 K and with the frequencies of the infrared modes. The usual frequencies of the normal modes of the octahedral entity $[\mathrm{CrF}_6]^{3-}$ were also considered.

---

[*] Permanent address: CNRS UPR211, 1, place A. Briand, 92195 Meudon Cedex, France.

[1] U. Brauch and U. Dürr, Opt. Commun. **49**, 61 (1984); Opt. Lett. **9**, 441 (1984); U. Brauch, Ph.D. thesis, University of Stuttgart, 1983.

[2] J. L. Patel, J. J. Davies, B. C. Cavenett, H. Takeuchi, and K. Horai, J. Phys. C **9**, 129 (1976).

[3] Y. Vaills, J. Y. Buzaré, and M. Rousseau, J. Phys. Condens. Matter **2**, 3997 (1990).

[4] R. K. Jeck and J. J. Krebs, Phys. Rev. B **5**, 1677 (1972).

[5] J. Y. Buzaré and J. C. Fayet, C.R. Acad. Sci. Ser. B **279**, 353 (1974).

[6] B. Villacampa, J. Casas Gonzales, R. Alcala, and P. J. Alonso, J. Phys., Condens. Matter. **3**, 8281 (1991).

[7] M. Mortier, J. Y. Gesland, B. Piriou, J. Y. Buzaré, and M. Rousseau, Opt. Mater. **4**, 115 (1994).

[8] V. W. Goldschmidt, J. Math. Naturvid. Klass **2**, 97 (1926).

[9] M. Rousseau, Ph.D. Thesis Université Paris 6, 1977.

[10] D. R. Lee, T. P. J. Han, and B. Henderson, Appl. Phys. A **59**, 365 (1994).

[11] O. Pilla, E. Galvanetto, M. Montagna, and G. Viliani, Phys. Rev. B **38**, 3477 (1988).

[12] P. T. C. Freire, O. Pilla, and V. Lemos, Phys. Rev. B **49**, 9232 (1994).

[13] O. Pilla, P. T. C. Freire, and V. Lemos, Phys. Rev. B **52**, 177 (1995).

[14] M. Mortier, Ph.D. Thesis Université Paris 6, 1994.

[15] U. Fano, Phys. Rev. **124**, 1866 (1961).

[16] J. F. Dolan, L. A. Kappers, and R. H. Bartram, Phys. Rev. B **33**, 7339 (1986).

[17] Y. Tanabe and S. Sugano, J. Phys. Soc. Jpn. **9**, 753 (1954).

[18] J. M. Breteau, Ph.D. Thesis Université Paris 6, 1986.

[19] F. Auzel and J. M. Breteau, J. Phys. (France) Colloq. **48**, C7-451 (1987).

[20] A. B. P. Lever, *Inorganic Electronic Spectroscopy* (Elsevier, Amsterdam, 1968).

[21] D. De Viry, Ph.D. Thesis Université Paris 6, 1989.

[22] R. R. Burns, *Mineralogical Applications of Crystal Field Theory*, 2nd. ed. (Cambridge University Press, Cambridge, 1993).

[23] M. Lax, *Symmetry Principles in Solid State and Molecular Physics* (Wiley, New York, 1974).

[24] R. M. Macfarlane, J. Chem. Phys. **39**, 3118 (1963).

[25] A. J. Wojtowicz, M. Grinberg, and A. Lempicki, J. Lumin. **50**, 231 (1991).

[26] R. E. Englman and B. Halperin, Ann. Phys. (Paris) **3**, 453 (1978).

[27] J. H. Van Vleck, Phys. Rev. **59**, 724 (1941).

[28] S. Salaun, M. Mortier, J. Y. Gesland, M. Rousseau, and B. Hennion, J. Phys. Condens. Matter **5**, 7615 (1993).

[29] C. H. Perry and E. F. Young, J. Appl. Phys. **38**, 4616 (1967).

[30] B. Villacampa, R. Cases, and R. Alcala, J. Lumin. **63**, 289 (1995).

[31] A. S. Barker, Jr., and A. J. Sievers, Rev. Mod. Phys. **47**, 1 (1975).